Princeton Plasma Physics Laboratory

PPPL-4032

PPPL-4032

Higher Order Lagrange Finite Elements in M3D

J. Chen, H.R. Strauss, S.C. Jardin,
W. Park, L.E. Sugiyama, G. Fu, and J. Breslau

December 2004

Prepared for the U.S. Department of Energy under Contract DE-AC02-76CH03073.

PPPL Report Disclaimers

Full Legal Disclaimer

Trademark Disclaimer

PPPL Report Availability

This report is posted on the U.S. Department of Energy's Princeton Plasma Physics Laboratory Publications and Reports web site in Fiscal Year 2005. The home page for PPPL Reports and Publications is: http://www.pppl.gov/pub_report/

Office of Scientific and Technical Information (OSTI):

Available electronically at: http://www.osti.gov/bridge.

Available for a processing fee to U.S. Department of Energy and its contractors, in paper from:

U.S. Department of Energy
Office of Scientific and Technical Information
P.O. Box 62
Oak Ridge, TN 37831-0062

Telephone: (865) 576-8401

Fax: (865) 576-5728

E-mail: reports@adonis.osti.gov

National Technical Information Service (NTIS):

This report is available for sale to the general public from:

U.S. Department of Commerce
National Technical Information Service
5285 Port Royal Road
Springfield, VA 22161

Telephone: (800) 553-6847

Fax: (703) 605-6900

Email: orders@ntis.fedworld.gov

Online ordering: http://www.ntis.gov/ordering.htm

Higher Order Lagrange Finite Elements in M3D

J. Chen [a] H. R. Strauss [b] S. C. Jardin [a] W. Park [a]
L. E. Sugiyama [c] G. Fu [a] J. Breslau [a]

[a] *PPPL, P.O. Box 451, Princeton, NJ 08543*
[b] *Courant Institute, NYU, 251 Mercer Street, NY 10012*
[c] *Massachusetts Institute of Technology, Cambridge, MA 02139*

Abstract

The M3D code [1] has been using linear finite elements to represent multilevel MHD on 2D poloidal planes. Triangular higher order elements, up to third order are constructed here in order to provide M3D the capability to solve highly anisotropic transport problems. It is found that higher order elements are essential to resolve the thin transition layer characteristic of the anisotropic transport equation, particularly when the strong anisotropic direction is not aligned with one of the Cartesian coordinates. The transition layer is measured by the profile width, which is zero for infinite anisotropy. It is shown that only higher order schemes have the ability to make this layer converge towards zero when the anisotropy gets stronger and stronger. Two cases are considered. One has the strong transport direction partially aligned with one of the element edges, the other doesn't have any alignment. Both cases have the strong transport direction misaligned with the grid line by some angles.

Key words: Lagrange higher order elements, anisotropic transport
PACS: 52.65.-y, 52.65.Kj
1991 MSC: 64N30, 74E10

1. Introduction

As pointed out in [2], misalignment between the mesh and the magnetic field often occurs in plasma modeling, and when not aligned, a numerical cross-flux can be generated that pollutes the solution. The numerical errors caused by such misalignment have been discussed in a number of studies in order to understand this spurious effect.

In [3] and [4], bilinear finite elements were used to treat a complex edge plasma. It was found that the finite element mesh must obey certain requirements, imposed by the anisotropy with regard to parallel and cross-field transport in the plasma edge region. In particular, the element has to have one or two edges aligned to the poloidal magnetic field in order to guarantee an accurate numerical solution. In order to do so, they introduced an Unstructured Mesh Generator to keep the average misalignment to a few degrees, and a Structured Flux-surface Fitted Mesh Generator to keep it well below one degree. It was also found in [2] that when using higher order finite differences, the misalignment has to be very small in order to avoid unacceptable numerical pollution in practical edge plasma modeling.

M3D [1] has been using linear finite elements [5] on an unstructured triangular mesh to represent multilevel MHD. It is now realized that upgrading M3D to use higher order elements will allow the code to also accurately compute highly anisotropic heat transport. Here we examine the second and third order Lagrange elements and focus on analyzing the numerical error associated with misalignment of these elements.

The model problem we consider is the steady-state anisotropic heat conduction equation [2] in 2D:

$$\nabla \cdot (\vec{\kappa} \nabla T) = 0. \tag{1}$$

Where T is the temperature and $\vec{\kappa}$ is the conductivity tensor. This can be written in the orthogonal coordinates (ξ, η) aligned with the transport axes as

$$\frac{\partial}{\partial \xi} \kappa_\xi \frac{\partial T}{\partial \xi} + \frac{\partial}{\partial \eta} \kappa_\eta \frac{\partial T}{\partial \eta} = 0. \tag{2}$$

Without loss of generality we assume $\kappa_\xi \gg \kappa_\eta$, so that the strong transport direction is aligned with ξ. Define the anisotropy rate as $A_\kappa \equiv \kappa_\xi / \kappa_\eta$.

Consider Cartesian coordinates (x, y) that are not aligned with the transport axes, and denote the misalignment angle between x and ξ is by θ_m. Equation (2) then has the form:

$$\frac{\partial}{\partial x} A \frac{\partial T}{\partial x} + \frac{\partial}{\partial y} B \frac{\partial T}{\partial y} + \frac{\partial}{\partial x} C \frac{\partial T}{\partial y} + \frac{\partial}{\partial y} C \frac{\partial T}{\partial x} = 0, \tag{3}$$

with

$$
\begin{aligned}
A &= \kappa_\xi \cos^2\theta_m + \kappa_\eta \sin^2\theta_m, \\
B &= \kappa_\xi \sin^2\theta_m + \kappa_\eta \cos^2\theta_m, \\
C &= (\kappa_\xi - \kappa_\eta) \sin^2\theta_m \cos^2\theta_m.
\end{aligned} \tag{4}
$$

We will solve Eq.(3) on a rectangle domain ABCD: $[0, L_x] \times [0, L_y]$ with Dirichlet boundary conditions, as shown in Fig. 1. For clarity, κ and θ_m are assumed to be constant over the domain.

2. Lagrange Higher Order Elements

The high order Lagrange basis functions on a triangle element are constructed using the barycentric coordinate (α, β), which are nonorthogonal coordinates. Any point P on the triangle is identified with coordinates $(\lambda_1, \lambda_2, \lambda_3)$ where $\lambda_1 = \alpha$, $\lambda_2 = \beta$, $\lambda_3 = 1 - \alpha - \beta$. Obviously,

$$\lambda_1 + \lambda_2 + \lambda_3 = 1.$$

The three vertices of the triangle are given by $(1, 0, 0), (0, 1, 0), (0, 0, 1)$ (figure 2(a)). λ_1 is the area of the triangle given by 3 vertices (v_2, P, v_3), λ_2 the triangle (v_3, P, v_1), and λ_3 the triangle (v_1, P, v_2).

The linear basis functions in a triangle element are

$$
\begin{aligned}
N_1 &= \lambda_1 \\
N_2 &= \lambda_2 \\
N_3 &= \lambda_3
\end{aligned} \tag{5}
$$

and the 3 nodes are located at the triangle vertices.

For the second order elements, the first 3 nodes are located at the vertices, and the next 3 nodes are located at the midpoint of each side. The vertices are numbered 1,2,3 in counterclockwise order. Between vertex 1 and 2 is node 4. Between vertex 2 and 3 is node 5. Between vertex 3 and 1 is node 6 (figure

2(b)). The Lagrange basis functions in terms of the linear basis are

$$
\begin{aligned}
N_1 &= \lambda_1(2\lambda_1 - 1) \\
N_2 &= \lambda_2(2\lambda_2 - 1) \\
N_3 &= \lambda_3(2\lambda_3 - 1) \\
N_4 &= 4\lambda_1\lambda_2 \\
N_5 &= 4\lambda_2\lambda_3 \\
N_6 &= 4\lambda_3\lambda_1.
\end{aligned}
\tag{6}
$$

For the third order elements, the first 3 nodes of the triangle are located at the vertices. The next 6 nodes are located 1/3 and 2/3 of the way down each side. The vertices are numbered 1,2,3 in the counterclockwise. Between vertex 1 and 2 are nodes 4 and 5. Between vertex 2 and 3 are nodes 6 and 7. Between vertex 3 and 1 are nodes 8 and 9. The last, bubble node, is inside the triangle, at the intersection of the straight lines connecting the nodes 4 and 7, nodes 5 and 8, as well as nodes 6 and 9 (figure 2(c)). The Lagrange basis functions in terms of the linear basis are

$$
\begin{aligned}
N_1 &= \lambda_1(3\lambda_1 - 1)(3\lambda_1 - 2)/2 \\
N_2 &= \lambda_2(3\lambda_2 - 1)(3\lambda_2 - 2)/2 \\
N_3 &= \lambda_3(3\lambda_3 - 1)(3\lambda_3 - 2)/2 \\
N_4 &= (9/2)\lambda_1\lambda_2(3\lambda_1 - 1) \\
N_5 &= (9/2)\lambda_1\lambda_2(3\lambda_2 - 1) \\
N_6 &= (9/2)\lambda_2\lambda_3(3\lambda_2 - 1) \\
N_7 &= (9/2)\lambda_2\lambda_3(3\lambda_3 - 1) \\
N_8 &= (9/2)\lambda_3\lambda_1(3\lambda_3 - 1) \\
N_9 &= (9/2)\lambda_3\lambda_1(3\lambda_1 - 1) \\
N_{10} &= 27\lambda_1\lambda_2\lambda_3
\end{aligned}
\tag{7}
$$

The basis functions have the Lagrange property

$$
N_i(\alpha_j, \beta_j) = \delta_{ij} \tag{8}
$$

where (α_j, β_j) are the values of (α, β) at the nodal points j. The coordinates

of the triangles are given by an isoparametric mapping

$$\begin{aligned} x &= \textstyle\sum_{i=1}^{N} x_i N_i \\ y &= \textstyle\sum_{i=1}^{N} y_i N_i \end{aligned} \tag{9}$$

where N is the number of the nodes in an element, Here $N = 3$ for linear, $N = 6$ for second order, $N = 10$ for third order elements.

A fundamental operator is the Poisson bracket

$$[a, b] \equiv \frac{\partial a}{\partial \alpha}\frac{\partial b}{\partial \beta} - \frac{\partial a}{\partial \beta}\frac{\partial b}{\partial \alpha}. \tag{10}$$

When a, b are expanded in basis functions N_i, we need to evaluate the bracket of linear basis functions. It is the tensor defined by

$$\epsilon_{kl} = [\lambda_k, \lambda_l] = \begin{pmatrix} 0 & 1 & -1 \\ -1 & 0 & 1 \\ 1 & -1 & 0 \end{pmatrix} \tag{11}$$

and then the bracket of basis functions has the form

$$E_{ij} = [N_i, N_j] = \sum_{kl} \frac{\partial N_i}{\partial \lambda_k}\frac{\partial N_j}{\partial \lambda_l}\epsilon_{kl}. \tag{12}$$

The fundamental integrals are the element contribution to the mass matrix and stiffness matrix,

$$\begin{aligned} M_{ij} &= \int\int N_i N_j dxdy \\ &= \int\int N_i N_j J d\alpha d\beta \\ S_{ij} &= \int\int \nabla N_i \cdot S(\xi,\eta) \nabla N_j dxdy \\ &= \int\int \nabla N_i \cdot S(\xi,\eta) \nabla N_j J d\alpha d\beta \end{aligned} \tag{13}$$

where $S(\xi, \eta)$ stands for A, B, or C given in Eq.(4), and J represents the Jacobian of the coordinate transformation between (x, y) and the barycentric coordinate (α, β),

$$J = [x, y] = \sum_{i,j=1}^{N} E_{ij} x_i y_j. \tag{14}$$

The evaluation of the stiffness matrix needs the following relations

$$\begin{aligned} \frac{\partial N_i}{\partial x} &= \frac{1}{J}[N_i, y] = \frac{1}{J}\sum_{j=1}^{N} E_{ij} y_j \\ \frac{\partial N_i}{\partial y} &= -\frac{1}{J}[N_i, x] = -\frac{1}{J}\sum_{j=1}^{N} E_{ij} x_j \end{aligned} \tag{15}$$

where x, y are expanded in basis functions by Eq.(9).

The integral in Eq.(13) has to be done numerically by evaluating the integration at a set of N quadrature points (α_a, β_a) and applying weights w_a at the quadrature points,

$$\int\int f(\alpha,\beta) d\alpha d\beta \approx \sum_{a=1}^{N} f(\alpha_a, \beta_a) w_a. \tag{16}$$

In the case that the quadrature points are the same as the nodal points, the Lagrange property gives a diagonal mass matrix. However, this approximation is not accurate enough in general. Perhaps it could be used for only the mass matrix, and a more accurate approximation used for stiffness matrix. Sets of Gaussian quadrature points and weights are given in [6].

3. Numerical Experiments

The numerical calculation is set up in parallel on a multi-processor with distributed memory using MPI. Two cases are to be discussed:

Case a, Fig. 1(a). T=0 on side [AD-DC]; T=1 on side [AB-BC]. The strong transport direction, ξ, is aligned with the grid diagonal [AC] instead of the grid line x. The misalignment angle is the angle BAC, $\theta_m = arctan(L_y/L_x)$. For infinite anisotropy, the exact solution becomes: $T = 0$ above the grid diagonal [AC]; $T = 1$ below the grid diagonal [AC]. and the width of the transition zone is zero. For a finite value of anisotropy, the exact solution introduces an internal layer which has non-zero transition width.

Case b, Fig. 1(b). We impose a shift of the alignment of the strong transport direction from the grid diagonal [AC] to the non-diagonal [EF] such that: T=1 on side [EA-AB-BF]; T=0 on side [ED-DC-CF]. The misalignment angle is given by $\theta_m = arctan((L_y - [AE] - [CF])/L_x)$. For infinite anisotropy, the exact solution becomes: $T = 0$ above the grid diagonal [EF]; $T = 1$ below the grid diagonal [EF]. and the width of the transition zone is zero. For a finite value of anisotropy, the exact solution introduces an internal layer which has a non-zero transition width.

The profile width defined in [2] is used to measure the transient layer. It is the half-width, w, between the contour lines with $T = 0.25$, and $T = 0.75$ measured along the y direction through the mid-point.

As shown in Fig. 3, the unstructured triangular mesh is formed by first dividing the rectangular domain ABCD into rectangular cells uniformly: $[0, N_x] \times [0, N_y]$. Then each of the rectangle grids is subdivided into two triangles such that the element has one edge aligned with the strong anisotropy direction on the lower-left and upper-right blocks for Type 1 b.c., given above. But if it is used with Type 2 b.c., there is no alignment.

Eq.(3) is solved first on Type 1 b.c.. Contours of T are plotted in Fig. 4 with anisotropy fixed at ($\kappa_\xi = 10^3$). Note that there are 7 contour lines drawn in each subplot. Counting from color green to red, they are $T = 0.125, T = 0.25, T = 0.50, T = 0.625, T = 0.75$, and $T = 0.875$ contour lines, respectively. This is the same for all the contour plots to be shown below.

The 1st row is calculated using first order elements (5) with increasing grid resolution. As the grid gets finer and finer, the profile width is reduced, but not significantly. A dramatic improvement starts in the 2nd row, which is the motivation of this work. In the 2nd row, you can see that the width gets much narrower. This is due to the second order elements defined in Eq.(6). The transition layer is represented much better, even on the coarsest grid, by the second order elements than it is on finest grids by first order elements. The 3rd row is obtained by applying the third order elements defined in Eq.(7). Clearly this layer is narrowed down to another new level.

In figure 5, the contour is plotted against the increasing anisotropy. Here κ_ξ takes the values $10^1, 10^3, 10^5, 10^7, 10^9$, while the grid resolution is fixed at 59×59. Third order elements have been applied. When the anisotropy increases, we see from the figure that the transition layer becomes narrower and narrower, converging towards zero. This is consistent with the exact solution, since for extreme cases when $\kappa_\xi \to \infty$, the width $w \to 0$.

For these cases, the strongly anisotropic diffusion direction was aligned with one of the element edges at the lower-left and upper-right blocks. We next consider the case when there is no alignment: i.e. the shifted Type 2 b.c.. The same calculations shown in Figs. 4 and 5 have been repeated and demonstrate the same characteristic behavior, as seen in Figs. 6 and 7. The numerical broadening depends weakly on grid resolution, but strongly on the order of the schemes applied. The transition layer again shows a convergence towards zero when the anisotropy increases.

The width of the transition layer given in Figs. 5 and 7 are measured using a matlab function written by M. V. Umansky. They are plotted against the anisotropy κ_ξ in Fig. 8. Clearly, the width is broadened for Type 2 b.c. where

no alignment exists at all. Line a is the width corresponding to linear elements with Type 1 b.c.; Line b is for third order elements with Type 1 b.c.; Line c is for third order elements with Type 2 b.c.. Due to the higher order and partial alignment, line b gives better convergence than line a. Line c is widened about 1.16 times by the pitch angle θ_m as compared to line b.

4. Conclusions and Future Works

The numerical solution of the highly anisotropic transport equations can be difficult when the computational grid is not aligned with the strong transport direction. A transition layer was introduced by the perpendicular conduction κ_η. Here we discussed using higher order Lagrange elements to resolve this thin layer. The calculations were carried out on 2 types of misalignments: one has one element edge partially aligned with the strong anisotropy direction; the other one has no alignment at all.

The numerical experiment shows that the higher order elements bring essential convergence of this layer toward zero when the anisotropy increases, which is expected according to the exact solution. On the other hand, some dependence on the pitch angle θ_m and grid resolution was observed, but in a much less significant manner for the type of mesh presented in Fig. 3.

In the near future, we will compare these results to the finite difference results given in [2] and study the profile width dependence of pitch angle and grid resolution when using the C^1 elements [7]. We also note that the Adapted Mesh Refinement (AMR) could be introduced in the thin interface layer in order to improve numerical efficiency .

Acknowledgements

This work is supported by US DoE contract DE-AC02-76CH03073. The authors acknowledge useful discussions with the M3D group and are grateful for useful discussions with M. V. Umansky and for his making matlab function available to us.

References

[1] W. Park et al, Nonlinear simulation studies of Tokamaks and STs, Nucl. Fusion **43** 483 (2003).

[2] M. V. Umansky, M. S. Day, and T. D. Rognlien, On Numerical Solution of Strongly Anisotropic Diffusion Equation on Misaligned Grids.

[3] R. Vesey and D. Steiner, A Two-Dimensional Finite Element Model of the Edge Plasma, J. Comp. Phys. **116** 300-313 (1994).

[4] R. Zanino, Advanced Finite Element Modeling of the Tokamak Plasmas Edge, J. Comp. Phys. **138** 881-906 (1997).

[5] H. R. Strauss and D. W. Longcope, An adaptive finite element method for magneto-hydrodynamics, J. Comput. Phys, **147** 318-336 (1998).

[6] D. A. Dunavant, Int. J. Num. Meth. Engng. **21** 1129-48 (1985). The tables can be found in at www.owlnet.rice.edu/ mech517/Books/n10.pdf.

[7] S. C. Jardin, A triangular finite element with first-derivative continuity applied to fusion MHD applications, J. Comp. Phys. **200** 133-152 (2004).

Figure 1. The boundary condition used to solve the anisotropic transport equation, $L_x = L_y = 1$. (a) T=0 is specified on side [AD-DC], T=1 on [AB-BC], so that the anisotropy direction is aligned with the grid diagonal [AC]. (b) The boundary condition is shifted, so that the anisotropy direction is aligned with the [EF]. T=0 is specified on side [ED-DC-CF], T=1 on [EA-AB-BF].

Figure 2. The Lagrange Basis functions: (a) first order, 3 vertices. (b) second order. 6 vertices, and (c) third order, 10 vertices.

Figure 3. Mesh on which the anisotropic transport equation is solved. One edge of triangles at the upper-left and lower-right block is aligned with the diagonal [BD]; one edge of triangles at the lower-left and upper-right block is aligned with the diagonal [AC]. Therefore, the strong anisotropy direction is aligned with one edge of the triangles at the 2 blocks: lower-left and upper-right.

Figure 4. The contour plots of T by different grid resolution, $29 \times 29, 39 \times 39, 49 \times 49, 59 \times 59$: (1) 1st row: first order elements. (2) 2nd row: second order elements. (3) 3rd row: third order elements. Type 1 b.c. is used, and $\kappa_\xi = 10^3$ is fixed. While the profile width is reduced by finer grids to some extent (looking from left-right at 1st row), the higher order schemes bring in essential improvement. (looking from up-down at each columns).

Figure 5. The contour plots of T at different $\kappa_\xi : 10^1, 10^3, 10^5, 10^7, 10^9$ by third order elements. Type 1 b.c. is used, and the grid resolution is fixed at 59×59. As the anisotropy is getting stronger and stronger, the profile width shows a convergence towards zero.

Figure 6. The contour plots of T by different grid resolution, $29 \times 29, 39 \times 39, 49 \times 49, 59 \times 59$: (1) 1st row: first order elements. (2) 2nd row: second order elements. (3) 3rd row: third order elements. Type 2 b.c. is used, and $\kappa_\xi = 10^3$ is fixed. Even if none of the triangle edges is aligned with the strong anisotropic transport direction, the higher order elements still show that the transient layer is represented better.

Figure 7. The contour plots of T at different $\kappa_\xi : 10^1, 10^3, 10^5, 10^7, 10^9$ by third order elements. Type 2 b.c. is used, and the grid resolution is also fixed at 59×59. Even if none of the triangle edges is aligned with the strong anisotropic direction, the narrow profile width is still resolved by the 2nd and 3rd order elements.

Figure 8. The profile width at different $\kappa_\xi : 10^1, 10^3, 10^5, 10^7, 10^9$ by first and third order elements. Line a : linear elements with Type 1 b.c.; Line b : third order elements with Type 1 b.c.; Line c : third order elements with Type 2 b.c..

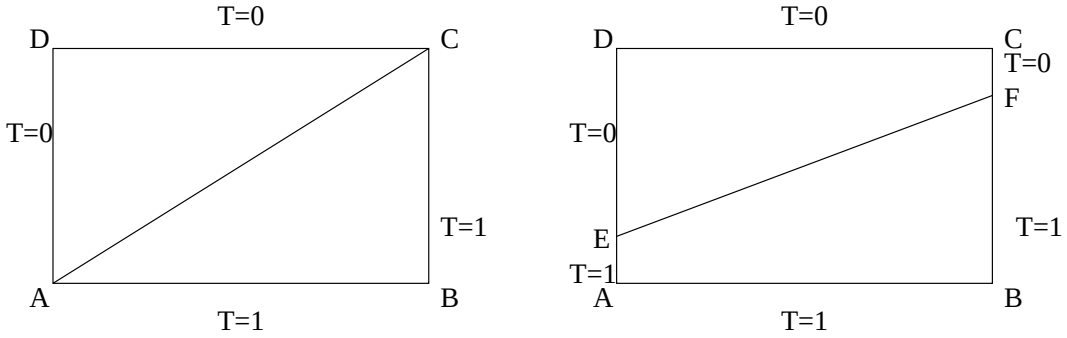

(a) (b)

Fig. 1.

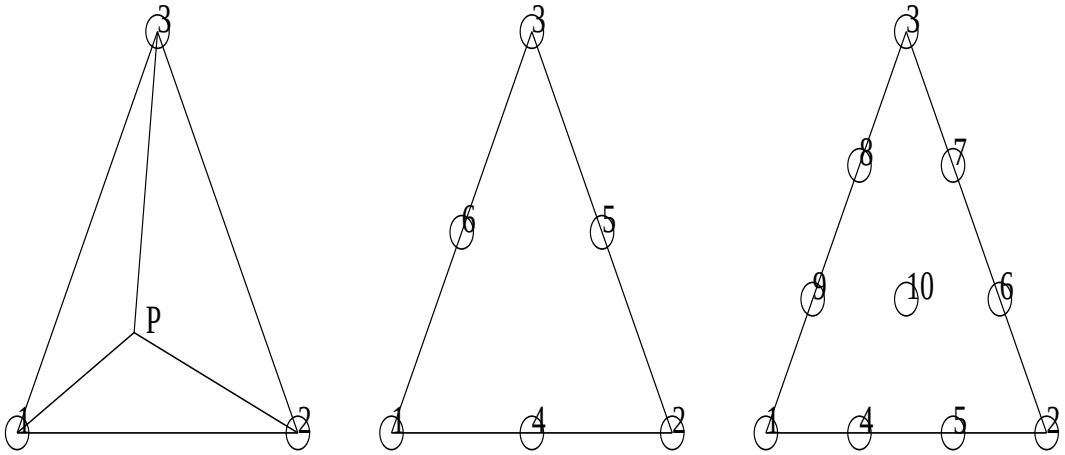

Fig. 2.

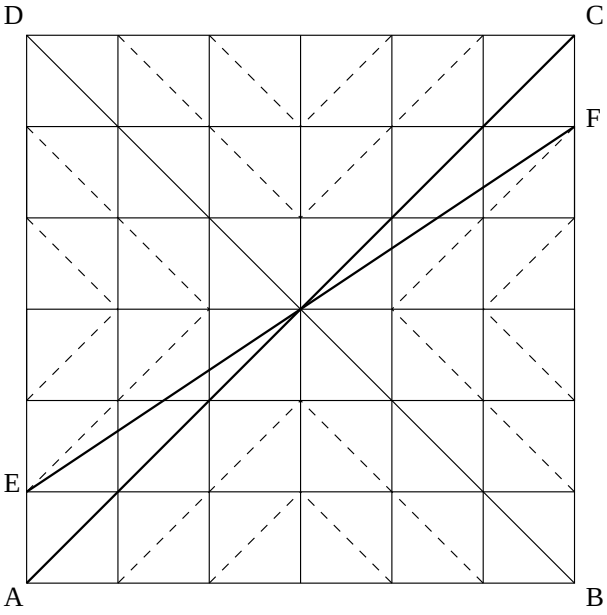

Fig. 3.

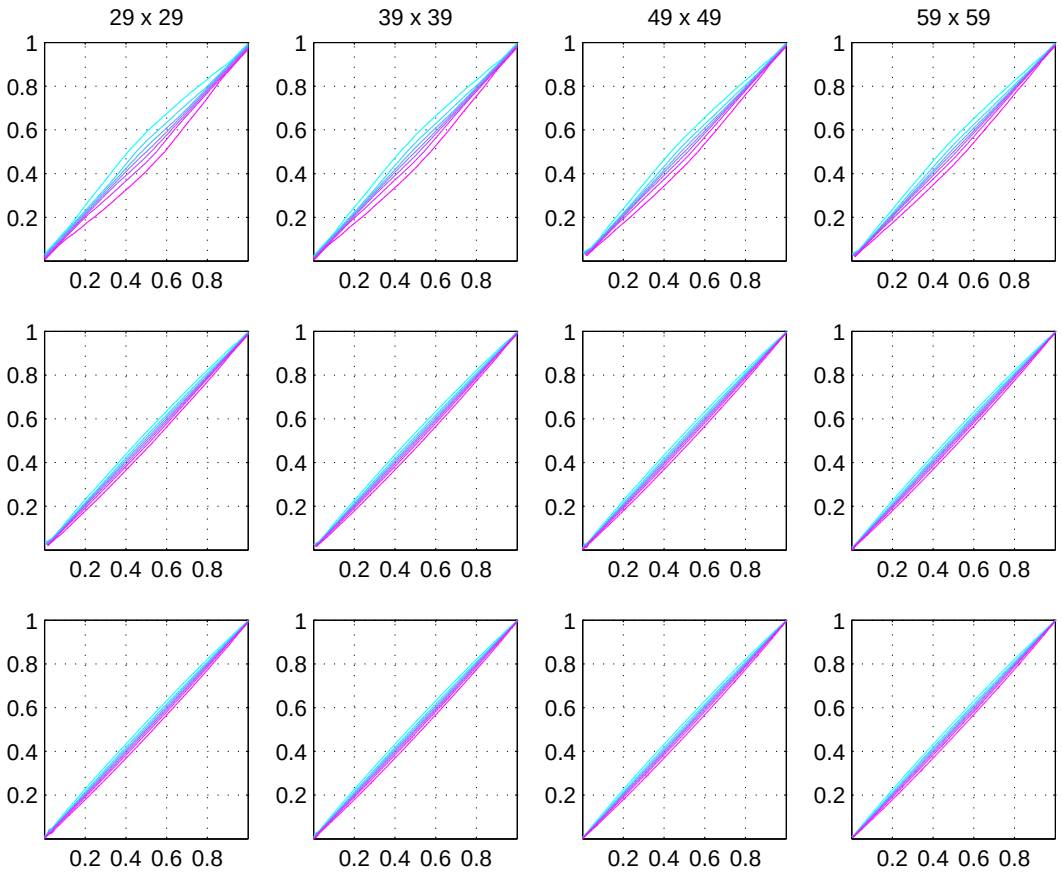

Fig. 4.

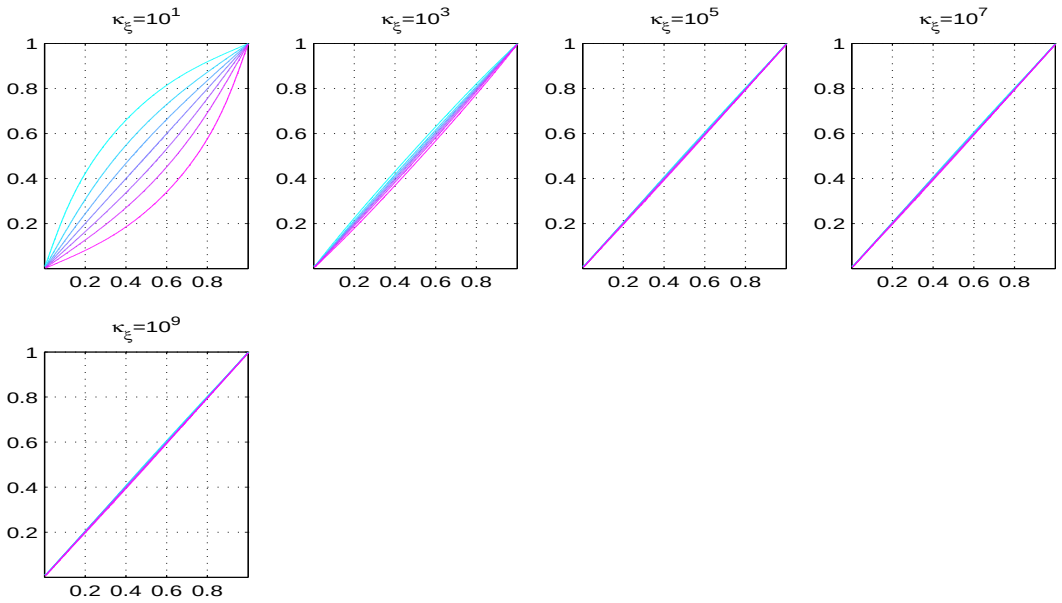
$\kappa_\xi=10^1$
$\kappa_\xi=10^3$
$\kappa_\xi=10^5$
$\kappa_\xi=10^7$
$\kappa_\xi=10^9$
1
0.8
0.6
0.4
0.2
0.2 0.4 0.6 0.8

Fig. 5.

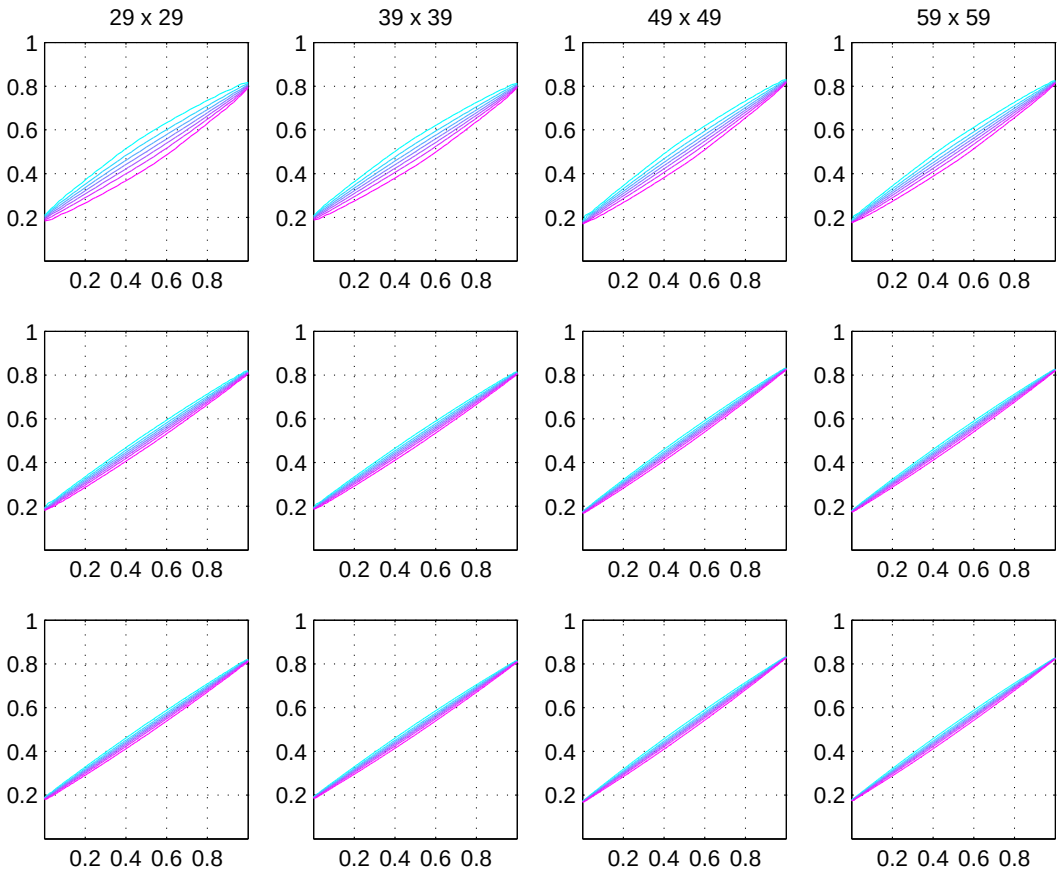

Fig. 6.

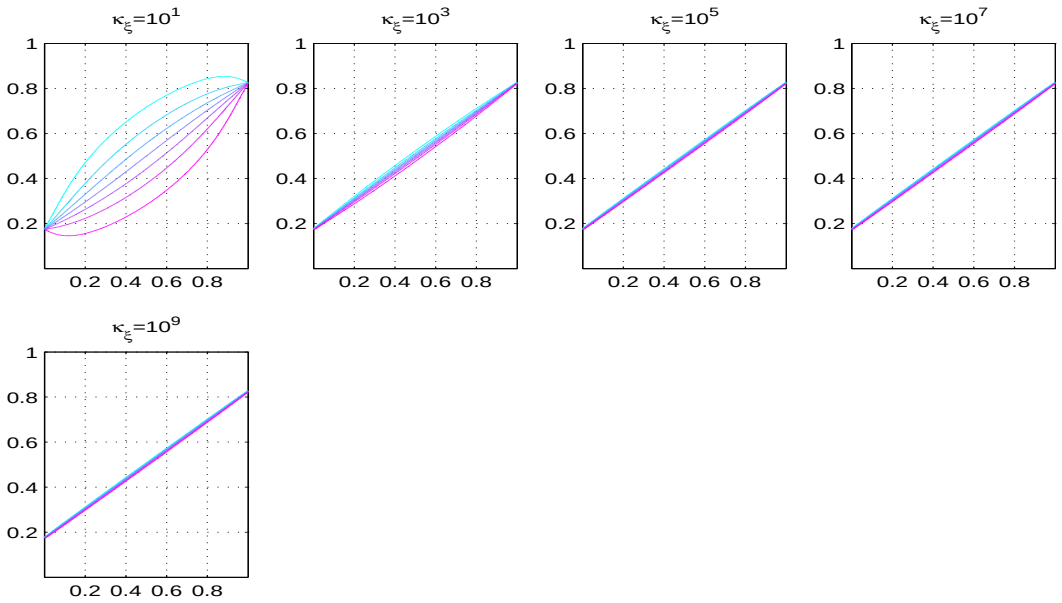
$\kappa_\xi=10^1$
$\kappa_\xi=10^3$
$\kappa_\xi=10^5$
$\kappa_\xi=10^7$
$\kappa_\xi=10^9$
1
0.8
0.6
0.4
0.2
0.2 0.4 0.6 0.8

Fig. 7.

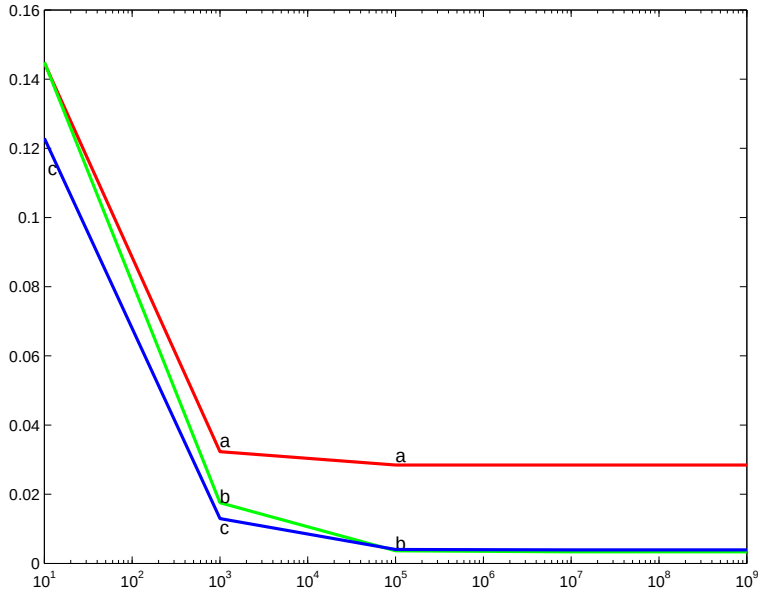
0.16
0.14
0.12
0.1
0.08
0.06
0.04
0.02
0
10^1
10^2
10^3
10^4
10^5
10^6
10^7
10^8
10^9
a
a
b
b
c
c

Fig. 8.

External Distribution

Plasma Research Laboratory, Australian National University, Australia

Professor I.R. Jones, Flinders University, Australia

Professor João Canalle, Instituto de Fisica DEQ/IF - UERJ, Brazil

Mr. Gerson O. Ludwig, Instituto Nacional de Pesquisas, Brazil

Dr. P.H. Sakanaka, Instituto Fisica, Brazil

The Librarian, Culham Laboratory, England

Mrs. S.A. Hutchinson, JET Library, England

Professor M.N. Bussac, Ecole Polytechnique, France

Librarian, Max-Planck-Institut für Plasmaphysik, Germany

Jolan Moldvai, Reports Library, Hungarian Academy of Sciences, Central Research Institute for Physics, Hungary

Dr. P. Kaw, Institute for Plasma Research, India

Ms. P.J. Pathak, Librarian, Institute for Plasma Research, India

Ms. Clelia De Palo, Associazione EURATOM-ENEA, Italy

Dr. G. Grosso, Instituto di Fisica del Plasma, Italy

Librarian, Naka Fusion Research Establishment, JAERI, Japan

Library, Laboratory for Complex Energy Processes, Institute for Advanced Study, Kyoto University, Japan

Research Information Center, National Institute for Fusion Science, Japan

Dr. O. Mitarai, Kyushu Tokai University, Japan

Dr. Jiangang Li, Institute of Plasma Physics, Chinese Academy of Sciences, People's Republic of China

Professor Yuping Huo, School of Physical Science and Technology, People's Republic of China

Library, Academia Sinica, Institute of Plasma Physics, People's Republic of China

Librarian, Institute of Physics, Chinese Academy of Sciences, People's Republic of China

Dr. S. Mirnov, TRINITI, Troitsk, Russian Federation, Russia

Dr. V.S. Strelkov, Kurchatov Institute, Russian Federation, Russia

Professor Peter Lukac, Katedra Fyziky Plazmy MFF UK, Mlynska dolina F-2, Komenskeho Univerzita, SK-842 15 Bratislava, Slovakia

Dr. G.S. Lee, Korea Basic Science Institute, South Korea

Institute for Plasma Research, University of Maryland, USA

Librarian, Fusion Energy Division, Oak Ridge National Laboratory, USA

Librarian, Institute of Fusion Studies, University of Texas, USA

Librarian, Magnetic Fusion Program, Lawrence Livermore National Laboratory, USA

Library, General Atomics, USA

Plasma Physics Group, Fusion Energy Research Program, University of California at San Diego, USA

Plasma Physics Library, Columbia University, USA

Alkesh Punjabi, Center for Fusion Research and Training, Hampton University, USA

Dr. W.M. Stacey, Fusion Research Center, Georgia Institute of Technology, USA

Dr. John Willis, U.S. Department of Energy, Office of Fusion Energy Sciences, USA

Mr. Paul H. Wright, Indianapolis, Indiana, USA

The Princeton Plasma Physics Laboratory is operated
by Princeton University under contract
with the U.S. Department of Energy.

Information Services
Princeton Plasma Physics Laboratory
P.O. Box 451
Princeton, NJ 08543

Phone: 609-243-2750
Fax: 609-243-2751
e-mail: pppl_info@pppl.gov
Internet Address: http://www.pppl.gov